© *A. A. Molkov*[1,2]*, 2022
© Translation from Russian: *E. S. Kochetkova*, 2022
[1]A.M. Obukhov Institute of Atmospheric Physics of the Russian Academy of Sciences,
119017, Pyzhevsky Per., 3, Moscow, Russia
[2]Institute of Applied Physics, Russian Academy of Sciences, 603950, Ulyanov Str., 46, Nizhny Novgorod, Russia
*E-mail: a.molkov@inbox.ru

QUALITATIVE ESTIMATION OF MODELED SNELL'S WINDOW STEREO IMAGERY FOR WIND WAVE PROFILE RETRIEVAL

Received 02.09.2021, revised 15.12.2021, accepted 10.01.2022

Abstract

On a qualitative level, the possibilities of using optical stereo images of the sea surface, registered from under the water, are considered in relation to the problem of remote diagnostics of waves. The task is implemented in a numerical experiment using a stereo image model of the Snell's window (underwater image of the sky) for a given relief of the sea surface. The influence of the camera parameters, observation geometry, illumination and excitement on the quality of constructing disparity maps, necessary to restore the distances to the sighted elements of the sea surface, is analyzed. Recommendations on the methodology of a full-scale experiment in order to test the proposed method are formulated.

Keywords: remote sensing, underwater imagery, stereo imagery, disparity, Snell's window, sea roughness, wind waves

© *А. А. Мольков*[1,2]*, 2022
© Перевод с русского: *Е. С. Кочеткова*, 2022
[1]Институт физики атмосферы им. А.М. Обухова РАН, 119017, Пыжевский пер., д. 3, г. Москва, Россия
[2]Институт прикладной физики РАН, 603950, ул. Ульянова, д. 46, г. Нижний Новгород, Россия
*E-mail: a.molkov@inbox.ru

КАЧЕСТВЕННЫЕ ОЦЕНКИ ВОЗМОЖНОСТИ ВОССТАНОВЛЕНИЯ ПРОФИЛЯ ВОЛНЕНИЯ ПО МОДЕЛЬНЫМ СТЕРЕОИЗОБРАЖЕНИЯМ КРУГА СНЕЛЛИУСА

Статья поступила в редакцию 02.09.2021, после доработки 15.12.2021, принята в печать 10.01.2022

Аннотация

На качественном уровне рассмотрены возможности использования оптических стереоизображений морской поверхности, зарегистрированных из-под воды, применительно к задаче дистанционной диагностики волнения. Задача реализована в численном эксперименте с использованием модели стереоизображения круга Снеллиуса (подводного изображения небосвода) для заданного рельефа морской поверхности. Проанализировано влияние параметров фотокамеры, геометрии наблюдения, освещения и волнения на качество построения карт диспарантности (смещения), необходимых для восстановления дальностей до визируемых элементов морской поверхности. Сформулированы рекомендации по методике проведения натурного эксперимента с целью апробации предложенного метода.

Ключевые слова: дистанционное зондирование, подводное видение, стереовидение, диспарантность, изображение морской поверхности, круг Снеллиуса, ветровое волнение, уклоны поверхности

1. Introduction

Registration and processing of sea surface images are among the most effective tools for reconstructing wave characteristics in a wide range of surface wave lengths [1–3]. Among the existing methods, specifically interesting is the stereophotogrammetrical method, based on the synchronous registration of a rough water surface

Ссылка для цитирования: *Мольков А.А.* Качественные оценки возможности восстановления профиля волнения по модельным стереоизображениям круга Снеллиуса // Фундаментальная и прикладная гидрофизика. 2022. Т. 15, № 1. С. 33–47. doi: 10.48612/fpg/p112-6ptf-fh5r
For citation: *Molkov A.A.* Qualitative Estimation of Modeled Snell's Window Stereo Imagery for Wind Wave Profile Retrieval. *Fundamental and Applied Hydrophysics.* 2022, 15, 1, 33–47. doi: 10.48612/fpg/p112-6ptf-fh5r

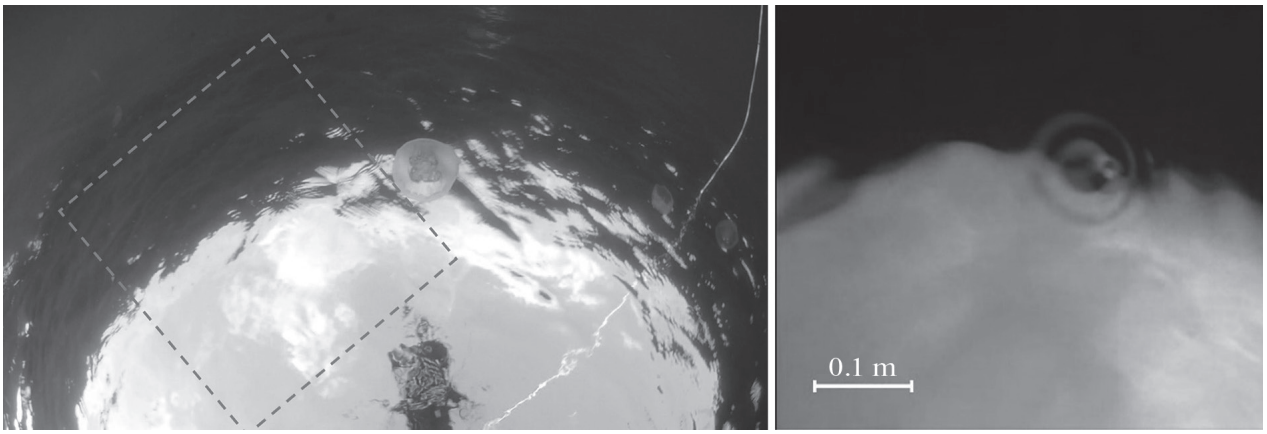

Fig. 1. Examples of the small-scale wave manifestation near the boundary of the Snell's window

section using two (or more) cameras and subsequent processing of stereo images employing known algorithms for retrieving the distance to surface elements through the disparity value [4–7]. Disparity (parallax) is the difference in the coordinates of the stereo pair pixels corresponding to the same object. Literature reports successful determination of long-wave components of wind waves with wavelengths up to tens of centimeters by this method. In this case, to resolve the corresponding waves, the image must contain markers of smaller scales, such as gravitational-capillary and capillary waves. There are no finer-scale natural markers on the water surface (breakings waves are not reliable). On the contrary, unfavorable lighting conditions or improperly chosen observation parameters make distinguishing capillary waves challenging. However, the small-scale waves with wavelengths of the order of millimeters may appear as high-contrast objects when observed from underwater at angles equal or close to internal reflection. Figure 1 shows examples of a wind ripple (left) and a raindrop falling in the water (right) at the outer borderof the Snell's window (an underwater image of the sky) [8].

In the absence of waves, the circle is outlined by a set of rays that fall on the sea surface tangentially and experience refraction at an angle $\beta_{Sn} = \arcsin(1/m) \approx 48{,}75°$ following Snell's law (here, $m \approx 1{,}33$ is the refractive index of water). The observed radiance of the image inside the circle depends on the water optical properties and the depth of the receiver. Approaching the circle boundary, the Fresnel reflection coefficient R_f tends to unity, and the radiance of the refracted light, proportional to $1 - R_f$, tends to zero. For this reason, the image of Snell's window looks like a light spot on a dark background. Waves change the local slope of the surface, leading to drastic variations in the Fresnel reflectance near the borderof the Snell's window. The mentioned algorithms for restoring wave parameters (slope variance and spectra) by statistic processing of a Snell's window image series were described in [9, 10]. Though the algorithms' efficiency and accuracy have not been established yet for natural conditions, there are two apparent features. The first feature is associated with the use of models, and hence approximations, when creating the mentioned algorithms (for example, neglecting surface elevations when calculating the underwater light field and the shading effect, etc.). The second feature is the need to process an array of high-resolution images (to distinguish small-scale waves), which is a resource-intensive process. The stereo imagery is devoid of these features and is therefore successfully used in a wide range of applications, including sea surface observations. For this reason, it is of particular interest to study the applicability of this method for viewing the sea surface from under the water. In this formulation, the problem is solved for the first time. Therefore, due to the lack of natural images, a preliminary assessment of the method capabilities is achieved by analyzing model images of the Snell's window obtained using a new augmented model of the Snell's window and pre-determined waves, neglecting the effects of light scattering in water. The paper presents a model of Snell's window stereo image; examples of calculating stereo images and disparity maps depending on the observation geometry, a set of camera parameters, waves, and lighting; and recommendations for the practical implementation of the method.

2. Methods and approaches

2.1. Assumptions

Realistic and, at the same time, mathematically accurate underwater images modeling is arduous and complicated, which, with all due diligence, can only be solved under a series of assumptions. The effect of the assumptions varies with the application between absolutely fundamental and insignificant. Determination of both by using preliminary works on underwater vision, together with stereo vision features in machine vision, appears a reasonable optimizing step from which it is necessary to start building the model of the Snell's window stereo image.

We assume that stereo images of the sea surface are formed by simultaneously recording the angular radiance distribution of the downwelling light using two identical synchronized ideal cameras with known characteristics. Ideal cameras suggest: no intrinsic noises; lens distortion is negligibly small; internal and external calibration of the stereo system, including image rectification, are not required (see, for example, [7]). The listed simplifications make it possible to skip several steps, mandatory in the processing of real stereo images, and proceed directly to calculating disparity maps necessary for the determination of a distance to the sighted elements of the sea surface.

At the moment, there is a variety of methods for calculating disparity, which differ in accuracy, speed, and principle of operation (see, for example, their comparative analysis in [11]). Finding the best method is crucial in machine vision applications where continuous real-time estimation of distances to objects is required. The purpose of this study is different, namely, to evaluate the general possibilities of using stereo images of the Snell's window to retrieve wave parameters. For this reason, we limited ourselves to using one widely accepted search method, namely Semi-Global Matching (SGM) [12], which provides a compromise between the quality of the results and the computation time. The main factors hindering the qualitative reconstruction of disparity maps include extended monotonous regions and abrupt changes in radiance (discontinuities). Both are present in sufficient numbers outside the Snell's window at low illumination, for example, in the evening (Fig. 1, *b*) or the central part of the window at a low sky radiance gradient and slight variations in the Fresnel reflectance (Fig. 1, *a*). Given the above, the optimal surface area occurs near the borderof Snell's window, combining a noticeable gradient in the sky radiance and sufficient illumination below the sea surface outside the window. An example of such a region is the region inside the rectangle marked with a dotted line in Fig. 1, *a*.

Inside the studied region, medium-sized patches are identified distinctly by a seemingly quasi-uniform radiance. However, upon a closer view, a unique small-scale notch formed by capillary disturbance is detected. Exactly due to the presence of this notch, the considered methods of correspondence determination lead to successful resolution of the longer-wavelength part of the waves in the sea surface relief, namely, the gravitational-capillary part. In its turn, the latter is a marker for resolving the even longer wavelength component, and so on. [7].

Apparently, the quality of the image reproduction in a numerical experiment, as shown in the selected fragment in Fig. 1, *a* and accounting the above-mentioned features, depends on the detailing the simulated sea surface. Traditionally, a superposition of cosine waves with a deterministic amplitude identified from the wave spectrum and a random phase is used. The shorter the waves are involved, the more resource-intensive the calculation becomes. At the same time, traditional questions the simulation results such as insufficient "sharpness" of waves remain with. At the same time, the need to study stereo images depending on a whole set of parameters leads to a necessity to simulate a large number of high-resolution scenes, which excluded this approach to wave modeling. The alternative was as follows.

2.2. Model of the sea surface roughness

We define the general surface topography by a single cosine wave — a swell wave with parameters (amplitude and wavelength) that are tunable in the course of experiments and propagating along the optical receivers' coordinate axis.

The image of a raindrop falling into the water in Fig. 1, *b* prompted the idea of objects of various scales falling into the water, generating divergent cylindrical waves of various intensity, length, and steepness. For this

Fig. 2. An example of a texture for creating small-scale irregularities on the sea surface (left) and its close-up view (right)

reason, the field of medium-scale inhomogeneities can be recreated by a set of cylindrical waves randomly scattered over a given coordinate grid and not changing their position from experiment to experiment. The length of the propagation region of each wave is set by the exponential law of damping.

We create the smallest-scale inhomogeneities by digitizing and scaling a small-scale texture as weak discontinuance in radiance, as shown in Fig. 2. Traditionally such textures are used in rendering systems to make modeled objects realistic. The obtained result is similar to the simulation of two-dimensional white noise, the intensity of which should be much less than the amplitude of medium-scale surface waves. The admissibility of the proposed approach is determined by the fact that, as noted above, in the stereo observation of the sea surface, the smallest-scale waves are a necessary element for reconstructing the longer-wavelength part. Consequently, when recalculating the reconstructed relief into a spectrum of elevations, the latter will be determined in the spectral interval that does not contain the shortest part of the wave, which simplifies the requirements for its modeling.

2.3. Snell's window model taking into account the upwelling light

Consider the instantaneous profile of a random rough water realization illuminated by unpolarized light: from above — by the light of the sky, from below — by the light upwelling from the water column (Fig. 3). The angular distribution of the radiance of the sky and the water column is determined by the functions $L_i^{\downarrow}\left(\mathbf{n}_i^{\downarrow}\right)$ and $L_i^{\uparrow}\left(\mathbf{n}_i^{\uparrow}\right)$ respectively, where $\mathbf{n}_i^{\downarrow}$ and $\mathbf{n}_i^{\uparrow}$ are the horizontal components of the unit vectors of the incident light on the sea surface from above and below, $\mathbf{\Omega}_i^{\downarrow}$ and $\mathbf{\Omega}_i^{\uparrow}$, respectively. The relief of the surface is characterized by the function of elevations $z = \zeta(\mathbf{r}_0)$ and the vector of slopes $\boldsymbol{\eta} = \mathbf{N}_{\perp}(\mathbf{r}_0)$, which is the horizontal component of the unit normal ($\mathbf{N}$) of the surface S at the point $\mathbf{r}_{\Sigma} = \mathbf{r}_0 + \zeta(\mathbf{r}_0)\mathbf{e}_z$ and is related to the function of its elevations by the relation $\boldsymbol{\eta} = \eta_x\mathbf{x}_0 + \eta_y\mathbf{x}_0 = -\Delta\zeta$ ($\mathbf{e}_z$ is the unit vector of the axis z, $\mathbf{r}_0$ is the radius vector of the projection of the point $\mathbf{r}_{\Sigma}$ on the plane $z = 0$). The optical properties of water are set by the refractive index m and attenuation coefficient c. We neglect the dependence of the water optical properties on the wavelength of light, temperature, and water salinity.

We consider that the image of the surface is formed using an optical receiver located at a point $\mathbf{r}_c$ at a depth Z_c and registering the angular radiance distribution of the light coming from the surface $L(\mathbf{n})$. The radiance is calculated in a universal form through the radiance of light at the interface "air-water" and the Green's function [14], using its simplest model, which completely ignores the contribution of light scattered by water. In this approximation, we do not estimate the upwelling light as a superposition of multiple scattering of the downwelling light. On the contrary, we assume it is deterministic and not subject to scattering. In particular, assuming the depth to be infinite (there is no bottom effect), we consider that the angular distribution of the upwelling radi-

ance is isotropic (see the equations below). This approach allows us to create an underwater light source necessary for illuminating the sea surface from below, significantly simplifying mathematical calculations and speeding up numerical calculations.

Further, applying the effective bordercondition for the radiance on the plane $z = 0$, which is often used in problems of optics of a rough water surface, ignoring the influence of surface elevations on the structure of the light field below the surface, and, leaving aside mathematical calculations, we arrive at the following set of formulas for the angular distribution of the Snell's window radiance $L(\mathbf{n})$ as a function of the horizontal component $\mathbf{n}$ of the unit vector $\grave{\mathbf{U}}$, characterizing the direction of light propagation in water (Fig. 4):

$$L(\mathbf{n}) = L_{sky}(\mathbf{n}) + L_{water}(\mathbf{n}), \tag{1}$$

where

$$L_{sky}(\mathbf{n}) = L_{sky}\big|_{z=0}\left(-\mathbf{n}Z/\sqrt{1-n^2}, \mathbf{n}\right)\exp\left\{-cZ/\sqrt{1-n^2}\right\} \tag{2}$$

– the radiance of the sky light refracted by the water surface,

$$L_{sky}\big|_{z=0}(\mathbf{r}_0, \mathbf{n}) = m^2\left(1 - R_F^{\downarrow}\left(\alpha_i^{\downarrow}(\mathbf{r}_0, \mathbf{n})\right)\right)L_i^{\downarrow}\left(\mathbf{n}_i^{\downarrow}(\mathbf{r}_0, \mathbf{n})\right) \tag{3}$$

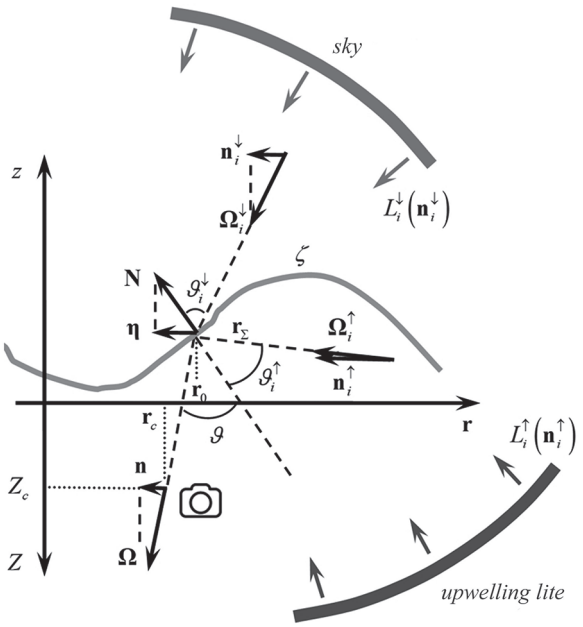

Fig. 3. A graphical diagram explaining the formation of the Snell's window image by the light of the sky and the light of the water column reflected by the sea surface into the lower hemisphere

– the radiance of the refracted light at the interface $z = 0$ at the point $\mathbf{r}_0 = -\mathbf{n}Z/\sqrt{1-n^2}$,

$$R_F^{\downarrow}\left(\alpha_i^{\downarrow}\right) = \frac{1}{2}\left[\left(\frac{\sqrt{1-\alpha_i^{\downarrow 2}} - \sqrt{m^2-\alpha_i^{\downarrow 2}}}{\sqrt{1-\alpha_i^{\downarrow 2}} + \sqrt{m^2-\alpha_i^{\downarrow 2}}}\right)^2 + \left(\frac{\sqrt{1-\alpha_i^{\downarrow 2}} - m^{-2}\sqrt{m^2-\alpha_i^{\downarrow 2}}}{\sqrt{1-\alpha_i^{\downarrow 2}} + m^{-2}\sqrt{m^2-\alpha_i^{\downarrow 2}}}\right)^2\right] \tag{4}$$

– Fresnel reflectance for unpolarized light,

$$\alpha_i^{\downarrow}(\mathbf{r}_0, \mathbf{n}) = \sin\vartheta_i^{\downarrow} = m\sqrt{1-\left(\sqrt{1-n^2}\sqrt{1-\eta(\mathbf{r}_0)^2} - \mathbf{n}\,\boldsymbol{\eta}(\mathbf{r}_0)\right)^2} \tag{5}$$

– the local angle sine of incidence expressed in terms of the local slope $\eta(\mathbf{r}_0)$ and the direction of the refracted light $\mathbf{n}$,

$$L_i^{\downarrow}\left(\mathbf{n}_i^{\downarrow}(\mathbf{r}_0, \mathbf{n})\right) = L_i^{\downarrow 0}\frac{1 + 2\sqrt{1-n_i^{\downarrow}(\mathbf{r}_0, \mathbf{n})^2}}{3} \tag{6}$$

– angular distribution of radiance over the sky under continuous cloudiness ($L_i^{\downarrow 0}$ is the radiance of the sky at the zenith),

$$\mathbf{n}_i^{\downarrow}(\mathbf{r}_0, \mathbf{n}) = \frac{m}{1+\eta^2}\left[\mathbf{n} + \sqrt{1-n^2}\boldsymbol{\eta} + \boldsymbol{\eta}\sqrt{\frac{1+\eta^2}{m^2} - \left(\mathbf{n} + \sqrt{1-n^2}\boldsymbol{\eta}\right)^2}\right] \tag{7}$$

– horizontal component of the unit vector of light incident from above on the sea surface $\boldsymbol{\Omega}_i^{\downarrow}$.

A similar set of formulas takes place for the second term (1), which determines the contribution to the radiance of the Snell's window from the surface reflected upwelling light from the water column:

$$L_{water}(\mathbf{n}) = L_{water}\big|_{z=0}\left(-\mathbf{n}Z/\sqrt{1-n^2},\mathbf{n}\right)\exp\left\{-cZ/\sqrt{1-n^2}\right\} \tag{8}$$

where

$$L_{water}\big|_{z=0}(\mathbf{r}_0,\mathbf{n}) = R_F^{\uparrow}\left(\alpha_i^{\uparrow}(\mathbf{r}_0,\mathbf{n})\right)L_i^{\uparrow}\left(\mathbf{n}_i^{\uparrow}(\mathbf{r}_0,\mathbf{n})\right) \tag{9}$$

– radiance of upwelling light reflected at the interface $z = 0$ at the point $\mathbf{r}_0 = -\mathbf{n}Z/\sqrt{1-n^2}$,

$$R_F^{\uparrow}\left(\alpha_i^{\uparrow}\right) = \frac{1}{2}\left[\left(\frac{m\sqrt{1-\alpha_i^{\uparrow 2}}-\sqrt{1-m^2\alpha_i^{\uparrow 2}}}{m\sqrt{1-\alpha_i^{\uparrow 2}}+\sqrt{m^2-\alpha_i^{\uparrow 2}}}\right)^2+\left(\frac{\sqrt{1-\alpha_i^{\uparrow 2}}-m\sqrt{1-m^2\alpha_i^{\uparrow 2}}}{\sqrt{1-\alpha_i^{\uparrow 2}}+m\sqrt{1-m^2\alpha_i^{\uparrow 2}}}\right)^2\right] \tag{10}$$

– Fresnel reflectance for unpolarized light,

$$\alpha_i^{\uparrow}(\mathbf{r}_0,\mathbf{n}) = \sin\vartheta_i^{\uparrow} = \sqrt{1-\left(\sqrt{1-n^2}\sqrt{1-\eta(\mathbf{r}_0)^2}-\mathbf{n}\,\boldsymbol{\eta}(\mathbf{r}_0)\right)^2} \tag{11}$$

– sine of the local angle of incidence,

$$L_i^{\uparrow}\left(\mathbf{n}_i^{\uparrow}(\mathbf{r}_0,\mathbf{n})\right) = L_i^{\uparrow 0} \tag{12}$$

– isotropic angular distribution of the radiance of the water column,

$$\mathbf{n}_i^{\uparrow}(\mathbf{r}_0,\mathbf{n}) = \frac{1}{1+\eta^2}\left[\mathbf{n}+\sqrt{1-n^2}\boldsymbol{\eta}+\boldsymbol{\eta}\sqrt{1+\eta^2-\left(\mathbf{n}+\sqrt{1-n^2}\boldsymbol{\eta}\right)^2}\right] \tag{13}$$

– horizontal component of the unit vector of light incident from above on the sea surface $\boldsymbol{\Omega}_i^{\uparrow}$.

In practice, instead of a variable **n** in the equation (1) and further, it is more convenient to use cylindrical coordinates (ϑ, φ, z) and Cartesian coordinates (x, y, z), related as:

$$n_x = -x/\sqrt{x^2+y^2+z^2},\ \ n_y = -y/\sqrt{x^2+y^2+z^2}, \tag{14}$$

$$\vartheta = \arcsin(n),\ \varphi = \mathrm{tg}(n_y/n_x). \tag{15}$$

The given set of equations describes the angular radiance distribution of the light descending from the surface, the sources of which are the sky light and the light of the water column, backscattered by the surface into the lower hemisphere.

2.4. Snell's window stereo image model

In this paper, we consider one of the possible schemes for underwater observation. For simplicity, its schematic representation is given on the example of a plane xz (Fig. 5). We consider that two cameras are located on a plane xz at the same depth Z_c at a distance (base) b from each other in the direction of the axis x, which coincides with the direction of wave propagation. The cameras are oriented at an angle β to the vertical axis and have a field of view determined by the angle 2α. The focal length of the cameras is equal to f, the size of the matrix is $m_x \times m_y$, the resolution of the matrix is $p_x \times p_y$, the crop factor is s. The length of the observed area by the first camera A_1B_1, and by the second is A_2B_2. The length of the section covered by both cameras is denoted by A_2B_1. Consider an arbitrary point D, whose position on the first matrix is characterized by a pair of coordinates (u_1, v_1), on the second it is (u_2, v_2). The connection between the direction to the sighted element of the sea surface and its coordinates (in pixels) on the image follows from the geometry in Fig. 4.

$$u_i = \frac{p_x}{m_x}\left(\frac{m_x}{2}-f\tan(\vartheta_i-\beta)\right), \tag{16}$$

$$v_i = \frac{p_y}{m_y}\left(\frac{m_y}{2}+f\frac{\tan(\varphi_i)}{\cos(\vartheta_i-\beta)}\right). \tag{17}$$

The calculations performed by equations (1)—(17) form the basis for calculating the stereo image of Snell's window. The difference between the coordinates of the same image element determines the sought disparity d.

2.5. Modeling

The modeling process of Snell's window stereo images was carried out step by step. Initially, the internal parameters of the camera were determined using the example of a typical Nikon D5100 SLR camera with a Nikkor 18–55 mm lens due to its regular use in our full-scale measurements: $2\alpha = 60°$, $f = 25$ mm, $m_x \times m_y = 23.6 \times 15.8$ mm, $p_x \times p_y = 2144 \times 1424$ pixels, $s = 1.5$. Next, the water parameters (attenuation coefficient and refractive index) and the external parameters of the camera (the immersion depth Z_c m and the angle of inclination β relative to the vertical (see the values in Table 1)) were set. The latter was most often determined by the value $\beta = \beta_{Sn} - 10°$, which made it possible to obtain in the frame a surface area of approximately the same length relative to the border of the Snell's window. The third step was to calculate the boundaries of the sighted area in Cartesian coordinates and set a uniform grid with a resolution of $p_x \times p_y$. The topography of the sea surface was calculated on a given coordinate grid. The positions of cylindrical waves were always fixed, but the swell parameters changed from experiment to experiment between two sets of values, providing not only a different wave scale but also their steepness (see Table 1). Next, the topography was transformed to the slope field $\boldsymbol{\eta}(\mathbf{r})$, which was used to plot the angular distributions of the apparent radiance of the surface, "registered" by each camera, using the equation (1). The last step was Snell's window stereo images' calculation using formulas (16) and (17).

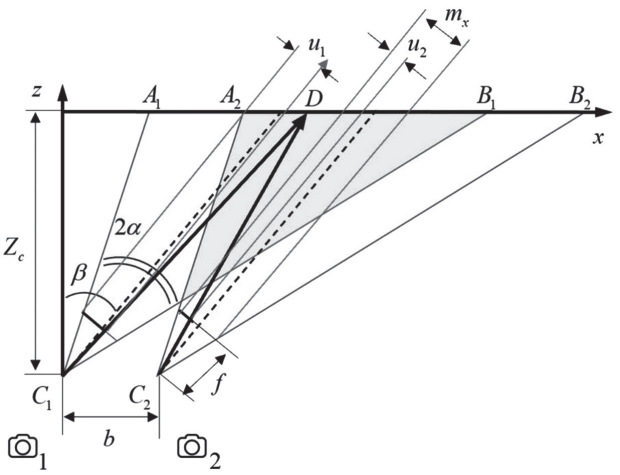

Fig. 4. Geometry of the sea surface observation by an underwater stereo system

Table 1

The main parameters and its values

Internal camera settings			
Field of view	30°; 60°		
Focal length	50 mm; 25 mm		
Matrix size	23.6 × 15.8 mm		
Resolution	2144 × 1424		
Crop factor	1.5		
External parameters of the stereo system			
Location depth	2 m; 5 m		
Stereo base	0.05 m; 0.2 m; 0.5 m		
Camera tilt from vertical	38.75°; 58.75°		
Wave parameters			
Swell wave	Amplitude, m	Length, m	Incline, °
	0.06	1	20
	0.006	0.3	8
Cylindrical waves	Amplitude, m	Length, m	Incline, °
No. 1	0.031	0.314	19
No. 2	0.019	0.128	27
No. 3	0.075	0.251	45
No. 4	0.013	0.251	10
No. 5	0.036	0.180	18

Fin table 1

No. 6	0.006	0.063	17
No. 7	0.013	0.063	33
No. 8	0.017	0.042	53
No. 9	0.013	0.126	18
No. 10	0.013	0.063	33
No. 11	0.189	0.628	44
No. 12	0.025	0.084	46
No. 13	0.075	0.251	43
No. 14	0.126	0.251	57
No. 15	0.126	0.628	33
Optical properties of water			
Refractive index	1.33 1/m		
Attenuation coefficient	0.33 1/m		
Parameters of the disparity search method			
Method	Semi-Global Matching (SGM)		
Range of disparity variations	128		
Search box	5 pixels		

As an example, Fig. 5 shows the result of calculating images with and without accounting for texture (small-scale waves).

3. Results and discussion

3.1. Angular distributions of apparent surface radiance

We should begin by presenting the results of calculation examples of apparent surface radiance using equation (1) at the depths of 2 m (Fig. 6) and 5 m (Fig. 7), considering various swell parameters. The solid arc marks the borderof the undisturbed Snell's window. The zenith and azimuth angles are plotted along the axes.

The relatively small size of the presented figures does not reflect fine details in the image structure but is sufficient to illustrate the radiance differences of the most extensive elements and the change in the shape of medium-sized light and dark spots (compared with dotted lines-arrows)up to their almost complete disappearance (compared with solid lines-arrows). Similar image pairs were used to construct disparity maps and evaluate their quality depending on parameter variations.

3.2. Disparity map and its variability with stereo base variations

Let us consider the results of calculating disparity maps using the example of two types of waves (the parameters are shown in Figs. 7 and 8) with three values of the stereo base — 0.05 m, 0.2 m, 0.5 m and two depth values of 2 m (Fig. 7) and 5 m (Fig. 8). The disparity scale is given in pixels. It is apparent that at a shallower depth and a small stereo base, about a third of the map area has no discontinuities, and divergent cylindrical waves can be traced in the structure.

As the base increases, the quality of the map drops, creating multiple gaps. The situation partly improves at greater depth. Here, with a small stereo base, the structure of the swell and the largest cylindrical waves are traced clearly, although the disparity variations are not substantial. As the base elongates, the number of gaps in the map increases, and information about cylindrical waves gets lost, but disparity variations associated with the swell increase. In practice, using special map post-filtering algorithms that eliminate discontinuities, the swell wave profile can be reconstructed in sufficient detail. With a further increase in the stereo base, the number of discontinuities grows correspondingly, while the correct disparity variations are observed at large distances, which retains the possibility of restoring the swell parameters from a remote image area. To obtain correct disparity values at short ranges, a repeat matching procedure for large disparity variations (256 or 512) is necessary, which may require a significant increase in the calculation time.

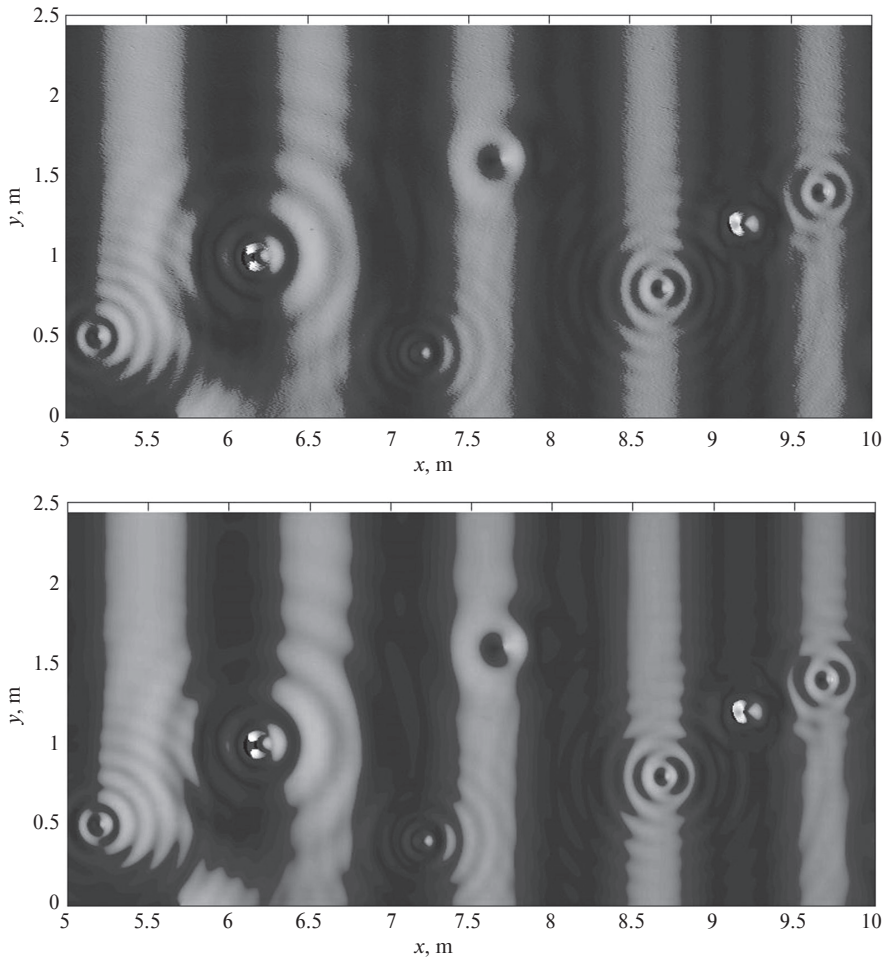

Fig. 5. An example of the simulated sea surface relief with small-scale irregularities (above) and without them (below)

3.2.1. Disparity map and its variability with variations in focal length (view angle)

According to the theory of stereo vision, the disparity grows linearly in proportion to the product of the stereo base and the focal length [15]. In this regard, and based on the obtained information on influence of the stereo base value, it seems interesting to evaluate the focal length variations effect. Consider a twofold increase in the focal length, accompanied by a narrowing of the field of view to 30° versus 60°. The dotted rectangles in the previously presented images of Snell's window (Fig. 7 and 8) demonstrate the shrinkage of the observed surface area. Detailed images of these areas are presented in the upper rows in Figs. 9 and 10. Comparison of disparity maps with the Figs. 7 and 8 allow us to conclude that the disparity variations have indeed doubled. The observed increase is most useful in terms of increasing the detail of the reconstructed sea surface relief when it is observed from a greater depth and with a small stereo base. With an average stereo base value, the disparity values at small viewing angles, i.e. at short range (within the border of the Snell's window), retreat as limitations. At the same time, both the shortest swell and cylindrical waves become distinguishable at large distances (figure on the right for the case $b = 0.2$ m). In the case of a longer stereo base, the disparity map is highly noisy and discontinuous and therefore is unlikely to be useful in solving the inverse problem.

3.2.2. Disparity map depending on the small-scale wave component

Let us consider the influence of the small-scale wave component, not traditionally modeled as white noise, on the quality of calculation of disparity maps using the example of two swell variants, two depths, and two stereo base values (Figs. 11 and 12). It is apparent that at a greater depth and a small stereo base, the structure of

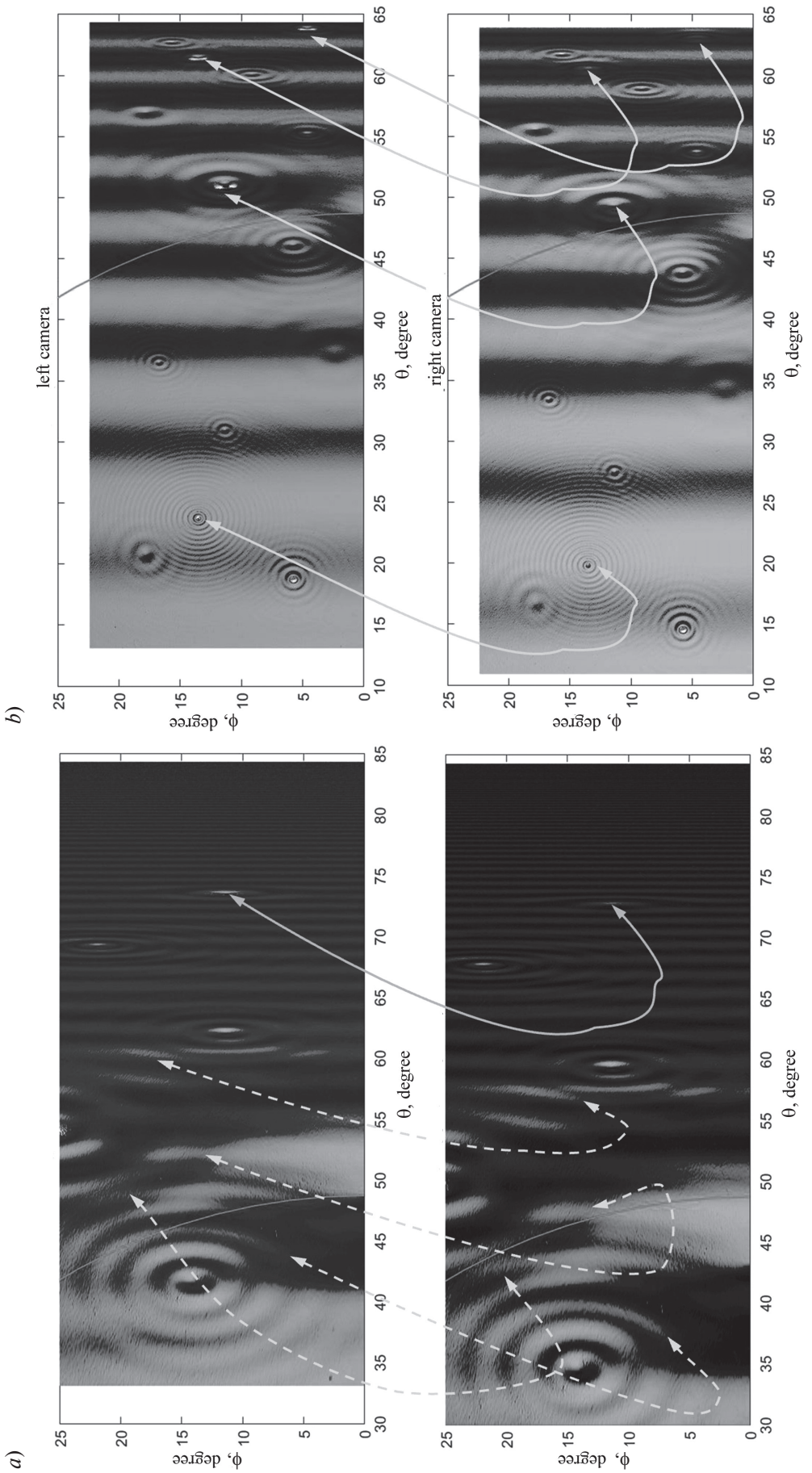

Fig. 6. Angular distributions of the sea surface radiance near the Snell's window, as seen by each of the cameras, from two depths — 2 m (*a*) and 5 m (*b*) with different swell parameters and camera orientation. *a* — depth is 2 m, stereo base is 0.2 m, swell wavelength is 0.3 m, swell amplitude is 0.02 m, camera inclination from zenith is 58.75°; *b* — depth is 5 m, stereo base is 0.2 m, swell wavelength is 1 m, swell amplitude is 0.06 m, camera inclination from zenith is 38.75°

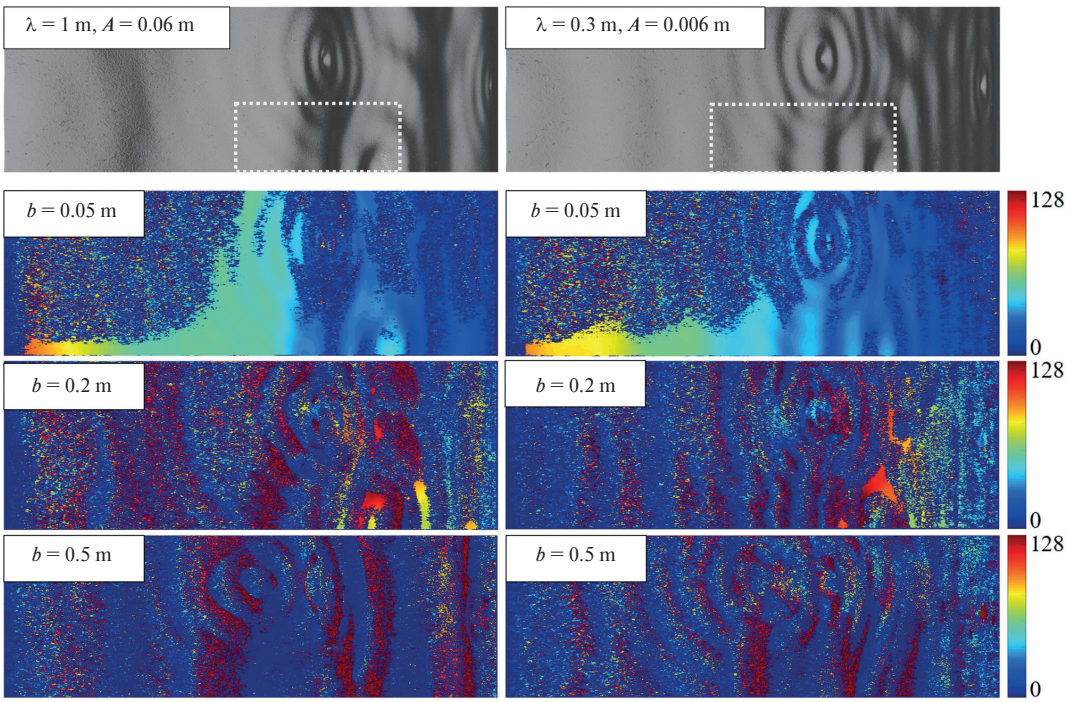

Fig. 7. The result of calculating the Snell's window images (top row) and disparity maps for a depth of 2 m, a field of view of 60°, three values of the stereo base (values are shown in the figure) and two swell options (parameters are shown in the figure). The disparity scale is presented in pixels

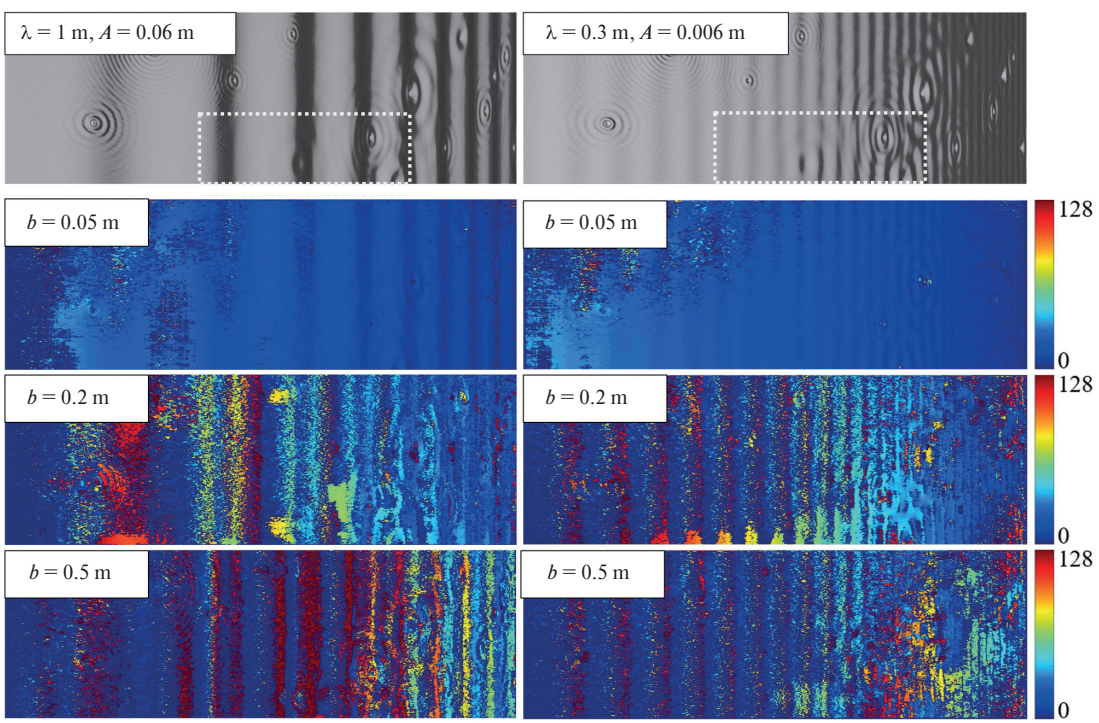

Fig. 8. The result of calculating the Snell's window images (top row) and disparity maps for a depth of 5 m, a field of view of 60°, three values of the stereo base (values are shown in the figure) and two swell options (parameters are shown in the figure). The disparity scale is presented in pixels

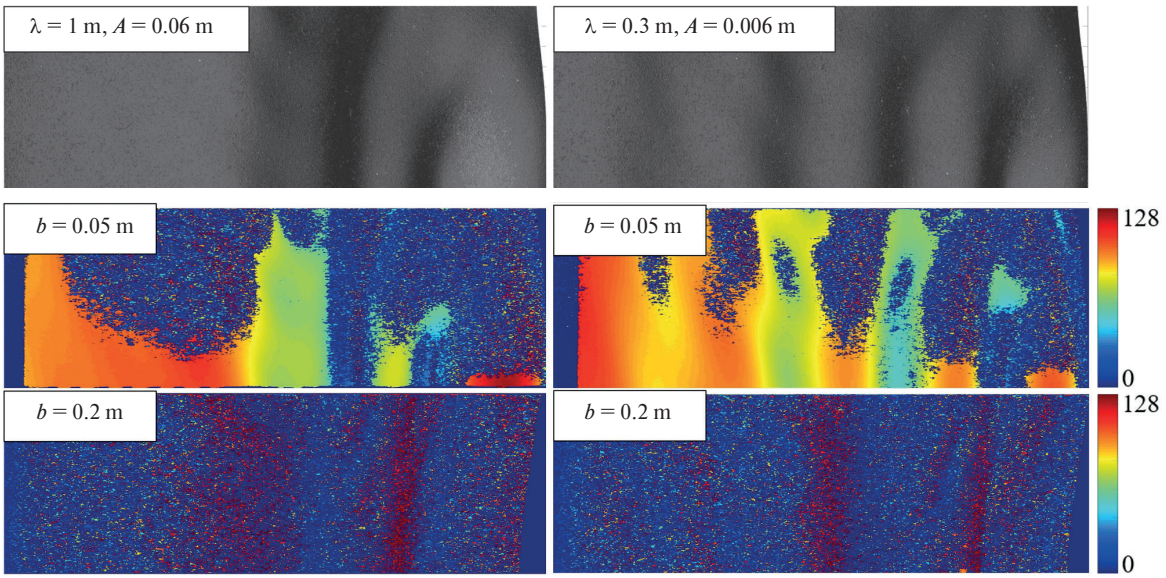

Fig. 9. The result of calculating the Snell's window images (top row) and disparity maps for a depth of 5 m, a field of view of 30°, three values of the stereo base (values are shown in the figure) and two swell options (parameters are shown in the figure). The disparity scale is presented in pixels

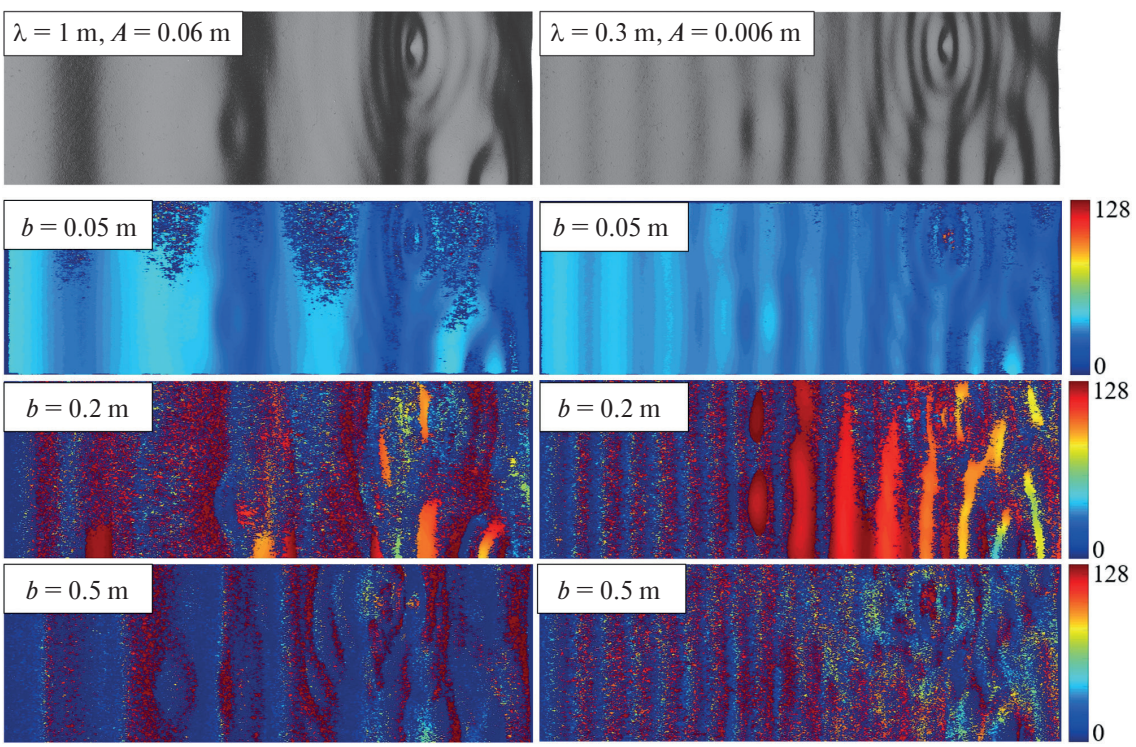

Fig. 10. The result of calculating the Snell's window images (top row) and disparity maps for a depth of 2 m, a field of view of 30°, three values of the stereo base (values are shown in the figure) and two swell options (parameters are shown in the figure). The disparity scale is presented in pixels

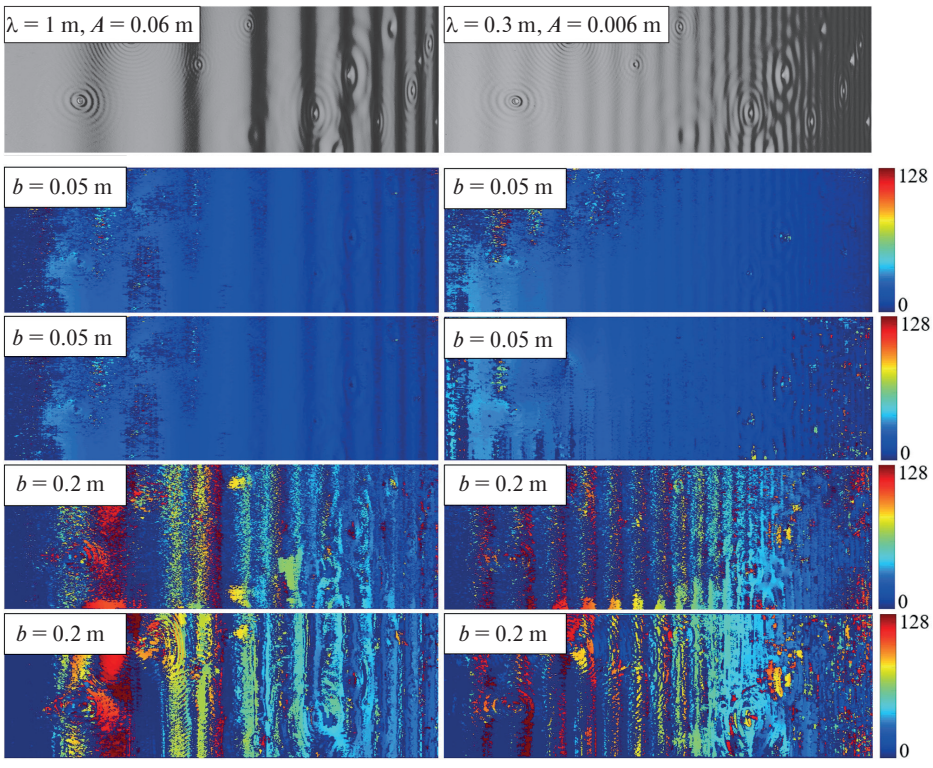

Fig. 11. The result of calculating the Snell's window images (row 1) and disparity maps, taking into account small-scale waves (rows 2 and 4) and without it (rows 3 and 5) for a depth of 5 m, two values of the stereo base (the values are shown in the figure) and two variants of swell (parameters are shown in the figure)

the map constructed without taking into account small-scale waves contains more noise, and the information about cylindrical waves is missing (Fig. 11, rows 2 and 3). At shallower depths, the situation is reversed (Fig. 12, rows 2 and 3). With a longer stereo base, in both cases, the best quality of disparity maps is observed when small-scale waves are neglected. Recoverable maps contain fewer gaps and do not require additional post-filtering. At the same time, it is interesting to note the manifestation of low-intensity cylindrical waves at short ranges in the structure of disparity maps for greater depth and bigger base (Fig. 11, row 5).

The demonstrated example indicates that, perhaps, the approach used with the representation of small-scale disturbances by white noise is not optimal due to insufficient spatial connectivity of neighboring elements of the "generated" wave. The answer to this question is planned in the next study, where, despite the time costs, we attempt to simulate waves over the widest possible spectral interval using traditional algorithms for modeling wind waves.

4. Conclusion

At the qualitative level, the paper studies the general possibility of Snell's window application for sea surface remote sensing. The problem is studied for the first time. Therefore, due to the lack of real images, the possibility of numerical calculation was used based on the proposed model of the stereo image of Snell's window. The mentioned possibility was evaluated by the quality of constructed disparity maps depending on the wave conditions, lighting, and camera and observation parameters also. The values of all parameters were chosen, as close as possible, to the real conditions and the photo cameras. Therefore, the calculation results are appropriate as preliminary auxiliary information for the efficient registration of Snell's window in real sea conditions. At the same time, the cameras were considered ideal, which made it possible to avoid the calibration of the stereo system and the rectification of images, which are necessary when working with real images.

The obtained results indicate that the method is applicable for recording the gravitational-capillary component of the waves from depths at which the influence of scattering and absorption of light in the water can be

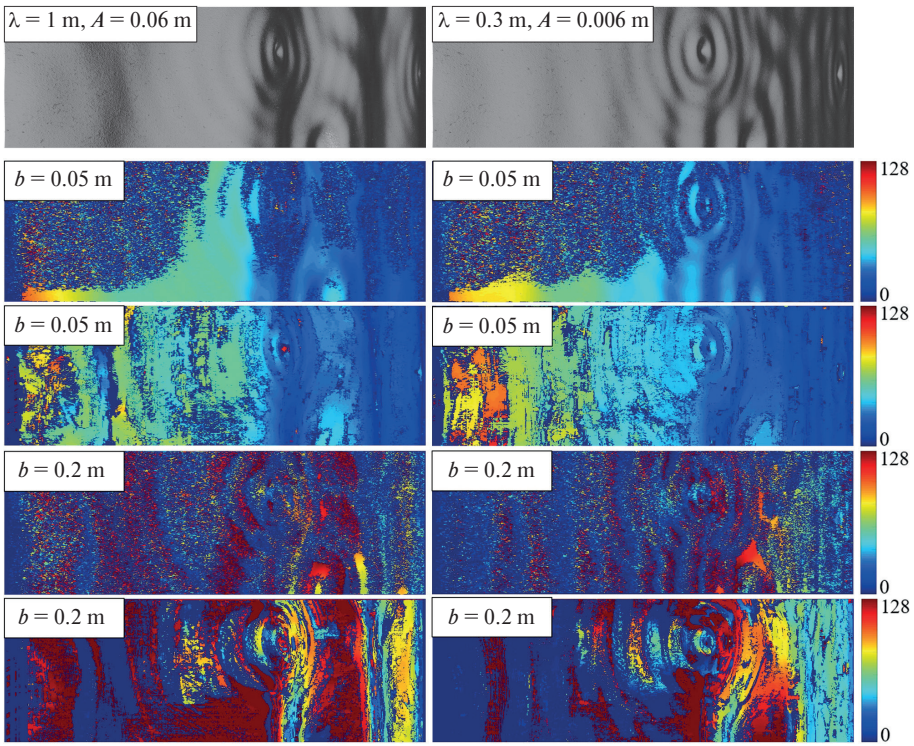

Fig. 12. The result of calculating the Snell's window images (row 1) and disparity maps, taking into account small-scale waves (rows 2 and 4) and without it (rows 3 and 5) for a depth of 2 m, two values of the stereo base (the values are shown in the figure) and two variants of swell (parameters are shown in the figure)

neglected. In this case, the image recording should be carried out in such a way that the radiance of the lower side of the sea surface outside the Snell's window border(when viewing at angles wider than the total internal reflection angle) is significant.

It is important to note that, in our opinion, due to the fact that the problem considered for numerical calculation is quite idealized, the issue of restoring the distances to surface elements through the presented disparity map should be solved using real images and take into account all the actions necessary for this, recommended by the theory of stereo vision. For this reason, this step was not considered in the present study but is planned in the future.

5. Funding

The reported study was funded by RFBR, project number 19-35-60034.

References

1. *Cox C.*, *Munk W.* Measurements of the Roughness of the Sea Surface from Photographs of the Sun Glitter. *Journal of the Optical Society of America*. 1954, 44, 838–850.
2. *Bakhanov V.V.*, *Demakova A.A.*, *Korinenko A.E.*, *Ryabkova M.S.*, *Titov V.I.* Estimation of the wind wave spectra with centimeters-to-meter lengths by the sea surface images. *Physical Oceanography* [e-journal]. 2018, 25(3), 177–190. doi: 10.22449/1573-160X-2018-3-177-190
3. *Kudryavtsev V.*, *Yurovskaya M.*, *Chapron B.*, *Collard F.*, *Donlon C.* Sun glitter imagery of ocean surface waves. Part 1: Directional spectrum retrieval and validation. *Journal of Geophysical Research*: *Oceans*. 122, 2017, 2, 1369–1383. doi: 10.1002/2016JC012425
4. *Banner M.L.*, *Jones S.F.*, *Trinder J.C.* Wavenumber spectra of short gravity waves. *Journal of Fluid Mechanics*. 1989, 198, 321–344. doi: 10.1017/S0022112089000157
5. *Shemdin O.H.*, *Tran H.M.* Measuring Short Surface Waves with Stereography. *Photogrammetric Engineering and Remote Sensing*. 1992, 58, 311–316.
6. *Benetazzo A.* Measurements of short water waves using stereo matched image sequences. *Coastal Engineering*. 2006, 53, 12, 1013–1032. doi: 10.1016/j.coastaleng.2006.06.012

7. *Kosnik M.V.*, *Dulov V.A.*, *Malinovskij V.V.*, *Smolov V.E.*, *Pogrebnoj A.E.* Estimation of two-dimensional spatial spectra of short waves using stereo photography. *Ekologicheskaya Bezopasnost' Pribrezhnoj i Shel'fovoj Zon i Kompleksnoe Ispol'zovanie Resursov Shel'fa*. 2009, 19, 401–414 (in Russian).
8. *Molkov A.A.*, *Dolin L.S.* Determination of wind roughness characteristics based on an underwater image of the sea surface. *Izvestiya. Atmospheric and Oceanic Physics*. 2012, 48, 552–564. doi: 10.1134/S0001433812050088
9. *Molkov A.A.* Retrieval of slope spectrum of sea roughness by Snell's window imagery: theory and numerical experiment (one-dimensional sea roughness). *Proc. SPIE11529*, *Remote Sensing of the Ocean*, *Sea Ice*, *Coastal Waters*, *and Large Water Regions* 2020, 115290C. doi: 10.1117/12.2573949
10. *Molkov A.A., Dolin L.S. Determination of the variance of rough water surface slopes be the distortions of Snell's circle boundary. Izvestiya. Atmospheric and Oceanic Physics. 2013, 49 (5), 567—577. doi: 10.1134/S0001433813050071*
11. *Vieira G. d. S.* et al. Stereo Vision Methods: From Development to the Evaluation of Disparity Maps. *2017 Workshop of Computer Vision* (WVC). 2017, 132–137. doi: 10.1109/WVC.2017.00030
12. MatLab. Block Matching. URL: https://nl.mathworks.com/help/vision/ref/blockmatching.html (date of access: 31.08.2021).
13. MatLab. Semi-Global Matching. URL: https://nl.mathworks.com/help/vision/ref/disparitysgm.html (date of access: 31.08.2021).
14. *Dolin L.S.*, *Levin I.M.* Theory of underwater vision. *Leningrad*, *Gidrometeoizdat,* 1991, 230 p. (in Russian).
15. *Hartley R.*, *Zisserman A.* Multiple view geometry in computer vision. *Cambridge University Press*, 2004. 700 p. doi: 10.1017/S0263574700223217

Литература

1. *Cox C.*, *Munk W.* Measurements of the Roughness of the Sea Surface from Photographs of the Sun Glitter// Journal of the Optical Society of America. 1954. No 44. P. 838–850.
2. *Баханов В.В.*, *Демакова А.А.*, *Кориненко А.Е.*, *Рябкова М.С.*, *Титов В.И.* Оценка спектров ветровых волн с длинами волн от сантиметров до метра по изображениям поверхности моря // Морской гидрофизический журнал, 2018. Т. 34, № 3. С. 192–205. doi: 10.22449/0233-7584-2018-3-192-205
3. *Kudryavtsev V.*, *Yurovskaya M.*, *Chapron B.*, *Collard F.*, *Donlon C.* Sun glitter imagery of ocean surface waves. Part 1: Directional spectrum retrieval and validation // Journal of Geophysical Research: Oceans 122. 2017. No 2. P. 1369–1383. doi: 10.1002/2016JC012425
4. *Banner M.L.*, *Jones S.F.*, *Trinder J.C.* Wavenumber spectra of short gravity waves // Journal of Fluid Mechanics. 1989. Vol. 198. P. 321–344. doi: 10.1017/S0022112089000157
5. *Shemdin O.H.*, *Tran H.M.* Measuring Short Surface Waves with Stereography // Photogrammetric Engineering and Remote Sensing. 1992. Vol. 58. P. 311–316.
6. *Benetazzo A.* Measurements of short water waves using stereo matched image sequences // Coastal Engineering. 2006. Vol. 53, No 12. P. 1013–1032. doi: 10.1016/j.coastaleng.2006.06.012
7. *Косник М.В.*, *Дулов В.А.*, *Малиновский В.В.*, *Смолов В.Е.*, *Погребной А.Е.* Оценка двумерных пространственных спектров коротких волн с помощью стереофотосъемки // Экологическая безопасность прибрежной и шельфовой зон и комплексное использование ресурсов шельфа, 2009, № 19. С. 401–414.
8. *Мольков А.А.*, *Долин Л.С.* Определение характеристик ветрового волнения по подводному изображению морской поверхности // Известия РАН. Физика атмосферы и океана, 2012. Т. 48, № 5. С. 617–630.
9. *Molkov A.A.* Retrieval of slope spectrum of sea roughness by Snell's window imagery: theory and numerical experiment (one-dimensional sea roughness) // Proceedings SPIE11529, Remote Sensing of the Ocean, Sea Ice, Coastal Waters, and Large Water Regions 2020, 115290C. doi: 10.1117/12.2573949
10. *Мольков А.А.*, *Долин Л.С.* Определение дисперсии уклонов взволнованной водной поверхности по размытию границы круга Снеллиуса // Известия РАН. Физика атмосферы и океана, 2013. Т. 49, № 5. С. 615–626. doi: 10.7868/S0002351513050076
11. *Vieira G. d. S.* et al. Stereo Vision Methods: From Development to the Evaluation of Disparity Maps // 2017 Workshop of Computer Vision (WVC). 2017. P. 132–137. doi: 10.1109/WVC.2017.00030
12. MatLab. Block Matching. URL: https://nl.mathworks.com/help/vision/ref/blockmatching.html (дата обращения: 31.08.2021).
13. MatLab. Semi-Global Matching. URL: https://nl.mathworks.com/help/vision/ref/disparitysgm.html (дата обращения: 31.08.2021).
14. *Долин Л.С.*, *Левин И.М.* Справочник по теории подводного видения. Ленинград: Гидрометеоиздат, 1991.
15. *Hartley R.*, *Zisserman A.* Multiple View Geometry in Computer Vision. Cambridge University Press, 2004. 700 p. doi: 10.1017/S0263574700223217